Optimization of quasi-β forging parameters to control trimodal microstructure parameters and performance of TC21 forgings

Xiang Li[1], Chaowen Huang[1]*, Jiang Yang[2], Fei Liu[1,3], Siyuan Wei[4], Mingpan Wan[1], Fei Zhao[1], Yongqing Zhao[5]*

[1]National and Local Joint Engineering Laboratory for High-Performance Metal Structure Materials and Advanced Manufacturing Technology, Guizhou University, Guiyang, 550025, China;

[2]School of Materials and Energy Engineering, Guizhou Institute of Technology, Guiyang, 550003, China;

[3]School of Mechanical and Aerospace Engineering, Nanyang Technological University, Singapore, 639798, Singapore;

[4]Institute of Materials Research and Engineering (IMRE) and Agency for Science, Technology and Research (A*STAR), Singapore, 138634, Singapore;

[5]Northwest Institute for Non-ferrous Metal Research, Xi'an, 710016, China;

*Corresponding author: cwhuang@gzu.edu.cn (C. Huang); trc@c-nin.com (Y. Zhao)

Abstract: This study aims to explore the influence of distinct forging parameters on microstructure and mechanical properties of TC21 forgings. The trimodal microstructure, which includes equiaxial α (α_{eq}), lath α (α_{lath}), and fine α (α_{fine}) phases, was achieved via quasi-β forging and dual heat treatment. Subsequently, mechanical properties were evaluated through tensile, impact toughness (a_k), and fracture toughness (K_{IC}) tests. Results indicate that the content of α_{eq} is higher at lower forging heating temperature, whereas the content of α_{lath} is diminished and the size of α_{fine} remains relatively small. This tendency reverses at higher forging heating temperature due to the increased driving force of the phase transition. The rise in α_{lath} content implies more pronounced interface strengthening and plastic deformation, which significantly contributes to strength compared to α_{fine} and α_{eq} but exerts a weaker influence on plasticity. Moreover, the combined deformation and fracture of α_{lath} and α_{fine} exert a significant influence on the initiation and propagation of cracks in a_k and K_{IC} specimens. The limited coordination of deformations exhibited by α_{lath} leads to preferential stacking dislocations and shear fractures at interfaces, which are further influenced by its higher aspect ratio affecting crack propagation paths. This not only increases the required energy for initiating cracks but also raises energy consumption during their propagation. Crucially, the presence of α_{fine} significantly enhances the dislocation accumulation and the plastic deformation zone at the crack tip, thereby playing a pivotal role in determining local deformation capacity and crack deflection frequency.

Keywords: TC21 forgings; quasi-β forging; forging parameters; trimodal microstructure; mechanical properties

1. Introduction

The TC21 titanium alloy plays a crucial role in aerospace structural materials owing to its exceptional strength, corrosion resistance and fatigue resistance [1]. As aerospace structure design shifts towards enhanced damage resistance, the use of components with superior mechanical properties in harsh environments becomes imperative [2, 3]. However, achieving a satisfactory match between the strength and toughness of TC21 forgings during service poses a persistent challenge, frequently resulting in premature component failure [4, 5]. Therefore, comprehensive research on the forging and forming process of TC21 forgings, along with the establishment of precise process parameters, is urgently needed to address this issue.

The influence of microstructure on mechanical properties of materials, particularly in titanium alloys, is widely recognized [6]. The composition, distribution, and morphology of α and β phases in these alloys are crucial for determining key material properties such as strength, fracture toughness (K_{IC}), creep behavior, fatigue resistance, and crack propagation resistance [7]. Consequently, current research primarily focuses on manipulating the microstructure through forging and heat treatment processes to improve overall macroscopic mechanical properties [8]. Notably, researchers have successfully developed a trimodal microstructure using near-β forging that incorporates equiaxed α (α_{eq}) phase, lath α (α_{lath}), and fine α (α_{fine}) phases. This unique configuration combines the strength of bimodal microstructure and basket-weave microstructure to offer exceptional plasticity, superior impact resistance, and enhanced crack resilience [9]. Furthermore, Shi et al. [10] discovered that increasing the residual β matrix content after near-isothermal forging enhances the strength of TC21 alloy, while the presence of coarse α laths aligned with the maximum resolved shear stress axis reduces its plasticity. Similarly, Zhou et al. [11] suggested that higher quasi-β forging temperatures lead to laths α phases coarsening, which promotes basket-weave microstructure formation and increases K_{IC} of TC21 alloy. Nevertheless, during the forging process, unfavorable factors inevitably introduce an uneven distribution of microstructure, emphasizing the critical role of subsequent heat treatment in optimizing it [12]. Solid solution and aging treatments are widely recognized for altering the size and morphology of α laths as well as secondary α lamellae, achieving a desirable balance between high strength and K_{IC} [13, 14]. Wang [15] and Tan [16] have suggested that increasing the solid solution temperature under fixed aging process could improve both hardness and strength of TC21 alloy. Furthermore, Wen et al. [17] discovered that the strength of TC21 alloy can be effectively enhanced by α colonies obtained through annealing after solid solution treatment. While there have been extensive studies on mechanical properties of TC21 titanium alloys, current research predominantly centers on elucidating microstructure evolution and enhancing performance [18, 19, 20, 21]. However, there is a notable gap in understanding how forging and heat treatment impact both strength and toughness of forgings [22, 23, 24]. More critically, comprehensive examinations of mechanical properties of TC21 forgings under trimodal microstructure parameters are lacking, and microstructural parameters for controlling the strength, plasticity, and toughness of TC21 forgings remains ambiguous. Hence, it is imperative to explore the evolution mechanism of the α phase within the trimodal microstructure under different forging parameters and to carefully adjust the characteristic parameters of the trimodal microstructure. These efforts are crucial in achieving an optimal balance of strength, plasticity, and toughness in components fabricated from TC21 alloy.

This study investigates the effects of forging heating temperature and holding time on microstructure and mechanical properties of TC21 forgings. Four types of quasi-β forging parameters were introduced in order to underscore the significance of microstructure evolution in thermo-mechanical processing. Furthermore, this work explores the mechanism of α phase evolution under different forging conditions. Simultaneously, the study also examines microstructure parameters of TC21 forgings to explore their correlation with strength, plasticity, and toughness. The objective is to identify crucial microstructural parameters that can control the strength, plasticity, and toughness of TC21 forgings. The results can provide reference and theoretical guidance for regulating microstructure and performance of TC21 forgings.

2. Experimental materials and methods

2.1 Materials and treatment process

The raw material was TC21 alloy provided by Northwest Nonferrous Metals Research Institute. The exact chemical composition of the alloy is given in Fig. 1a, and its microstructure comprises the α phase (α-Ti) and β phase (β-Ti). The β transition temperature, determined via metallographic analysis, was measured to be 971 ± 3 °C. Following preheating at 931°C for 49 minutes, four identical specimens underwent heating treatments using different processes. The heating and forging conditions adhered to those outlined in Table 1, precluding any return to the furnace for additional heating. The forging process was conducted on a 400 MN large die forging hydraulic press, with a forging pressure of about 150 MN and a deformation rate of 8 mm/s. The initial forging temperature was set at 976 °C, with a final forging temperature of ≥ 820 °C. Following this, test specimens were extracted from the quasi-β forged specimens and underwent heat treatment (solution and aging) in a high temperature tube furnace.

Table 1. Forging heating temperature and holding time

Specimens	Heating temperature	Forging temperature	Actual heating temperature
A	931 °C × 49 minutes with the furnace heating to 976 °C × 25 minutes	Start forging temperature 976 °C Final forging temperature ≥820 °C	976 ± 1 °C
B	931 °C × 49 minutes with the furnace heating to 976 °C × 50 minutes	Start forging temperature 976 °C Final forging temperature ≥820 °C	976 ± 1 °C
C	931 °C × 49 minutes with the furnace heating to 986 °C × 25 minutes	Start forging temperature 986 °C Final forging temperature ≥820 °C	986 ± 1 °C
D	931 °C × 49 minutes with the furnace heating to 986 °C × 50 minutes	Start forging temperature 986 °C Final forging temperature ≥820 °C	986 ± 1 °C

The solution treatment was conducted in a high-temperature Class III furnace at a temperature of 900 °C for 90 minutes, followed by air cooling (AC). Subsequently, the aging treatment took place in a Class II high-temperature electric furnace at a temperature of 590 °C for 240 minutes, also followed by AC (Figs. 1b to 1c). Furthermore, for clarity in discussing various mechanical properties of TC21 forgings under different forging conditions, the specimens from the four distinct forging parameters are denoted as specimens A, B, C, and D, as presented in Table 1.

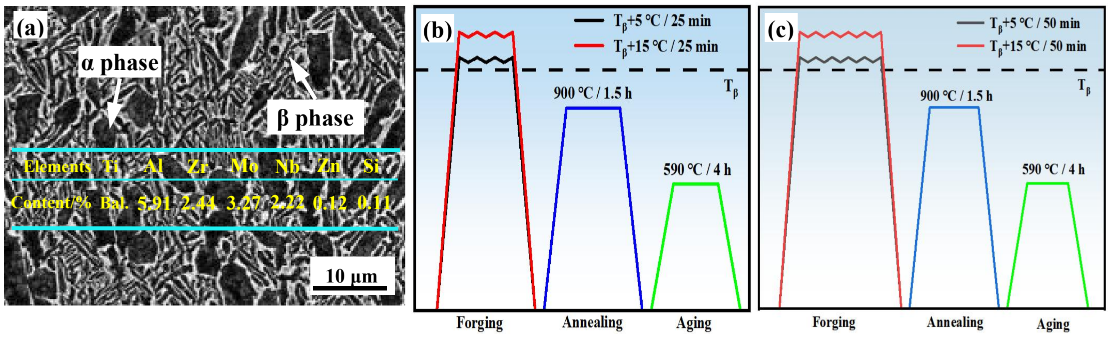

Fig. 1. (a) Original microstructure and chemical composition of TC21 alloy; (b) and (c) schedules of TC21 alloy at different quasi-β forging parameters and heat treatment process.

2.2 Mechanical properties testing

Quasi-static tensile tests were carried out on an MTS 810 universal tester equipped with an extensometer at a controlled rate of 1 mm/min at room temperature. The diameter of the parallel end of the tensile specimen was 5 mm, the length of the parallel end was 40 mm, the diameter of the clamping end was 10 mm, and the length of the clamping end was 30 mm (Fig. 2a). The compact tensile (CT) specimen of K_{IC} was tested using the MTS instrument, with specimen thickness B= 25 mm, width W= 50 mm (Fig. 2b). The crack was prefabricated with sine wave loading, the stress ratio R= 0.1 and the length of the minimum prefabricated crack was greater than 1.3 mm or 2.5% W, and the ratio of crack growth length (a) to W is about 48%. Finally, Charpy-V impact energy was measured by an NI300C pendulum impact testing machine with V-notch standard specimens (2 mm depth) in the dimension of 10 mm × 10 mm × 55 mm (Fig. 2c). For the impact test, specimens were extracted from CT specimens that had undergone K_{IC} testing. To ensure data authenticity and validity, three parallel specimens per state were tested and their average values were obtained.

2.3 Microstructure characterization

The microstructure, fracture morphology and fracture profile were analyzed using various techniques such as optical microscopy (OM, Leica DMI5000M), scanning electron microscopy (SEM, SUPRA40) and laser scanning confocal microscopy (LSCM, OLS500). Quantitative measurements of α phase dimensions (length and width) and content of specimens after different processes were performed using Image Pro Plus 8.0 (IPP 8.0) analysis software. To ensure statistical accuracy, a minimum of 10 images per state were quantitatively analyzed. Furthermore, the features of the microstructure deformation close to the crack initiation region of the a_k specimens were characterized via transmission electron microscopy (TEM, FEI Tecnai G2 F20), to study the microstructural deformation mechanism during impact process. The TEM foils were first mechanically ground to a thickness of ~0.08 mm and then further thinned using a Gatan 691 ion thinning instrument. The inclination angles of the three thinning stages were 8°, 5°, and 3°, and the working voltages were 5.3, 4.5, and 3.6 keV, respectively. The roughness of the fracture surfaces of CT specimens was measured using a LSCM to reveal the relationship between the roughness of the crack extension path and the K_{IC}. Meanwhile, ABAQUS software was used to analyze the crack propagation behavior of specimens after different forging processes.

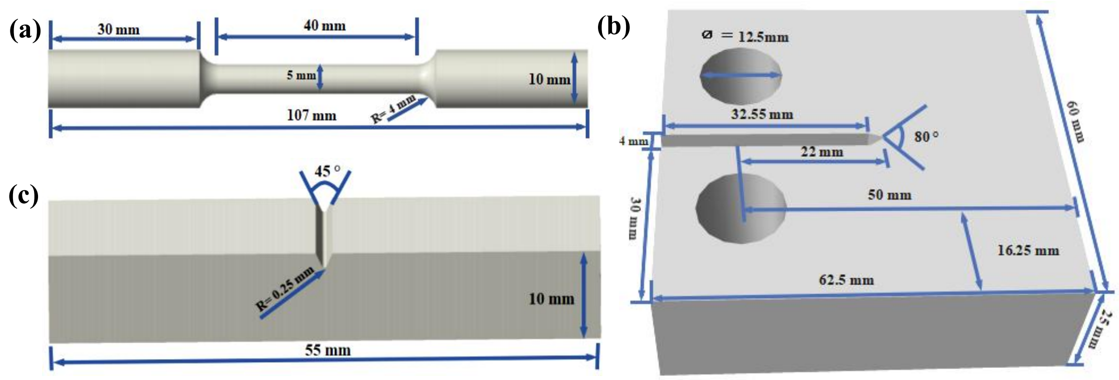

Fig. 2. (a) Standard tensile specimen schematic; (b) schematic diagram of CT specimen for K_{IC}; (c) the size of Charpy V-notch specimens for a_k.

3. Results

3.1 Effect of different forging parameters on microstructural characteristics

Microstructural evolution and characteristics of TC21 forgings through various quasi-β forging processes and without heat treatment are depicted in Fig. 3a. As the forging heating temperature increases, the trimodal microstructure resulting from the forging processes becomes more compact. The area of the local heterogeneous region gradually decreased, as depicted in the yellow region of Fig. 3a. After the forging of specimens A and B, their microstructure is mainly composed of equiaxed α phase with a minor presence of lath α phase. In contrast, specimens C and D exhibit a significant quantity of lath α phase, accompanied by a smaller proportion of equiaxed α phase [25]. Figs 3b to 3h illustrates the characteristics and statistical results of microstructure after quasi-β forging and double heat treatment. To further explore the effect of the quasi-β forging processes with the same heat treatment on the microstructure. Multiple images (at least 10 images) were quantitatively analyzed and and identified using the IPP 8.0 software to ensure the statistical accuracy of the results, and the obtained microstructure parameters are listed in Figs. 3e to 3g. The α phase with an aspect ratio below 1.5 is identified as α_{eq}. The microstructural homogeneity was optimized after heat treatment. As the forged heating temperature approaches the phase transition temperature (T_β + 5 °C), an incomplete transformation from the equiaxial α phase to the β phase leads to the presence of residual α_{eq}, which significantly affects the content of α_{eq}, especially noticeable at lower forging heating temperatures. Specimens A and B show similar driving forces of the phase transition under identical initial forging heating temperature conditions. However, a longer holding times allows the alloy to maintain a stable temperature near the phase change point,while facilitates more α phase transition into β phase. Subsequent heat treatment processes are carried out below the phase change point, causing atomic rearrangement in the matrix, thereby facilitating the precipitation and coarsening of the α phase [12]. However, specimen B demonstrates a more pronounced nucleation driving force compared to specimen A, resulting in preferential precipitation of a significant amount of α_{lath} during forging deformation while reducing the content of α_{eq}.

Similarly, the increase in the forging heating temperature (T_β + 15°C) provides more driving force of phase transition for the subsequent forging process or heat treatment process, which facilitates the formation of α_{lath} in the forging deformation process. Prolonging the holding time exacerbates the formation of α_{lath}, despite it being unfavorable for the presence of α_{eq}. Moreover, the higher forging heating temperature increases the diffusion ability of the β phase boundary. The continuous growth of grains occurs through the incorporation of adjacent grain boundary associated α phases pressed into strips. These adjacent α phases begin to contact and merge with each other, resulting in 'island chain like microstructure' distributions. During the forging heating process, the α phase dissolves into the β phase due to its higher Gibbs free energy. Subsequently, in synergy with AC and phase equilibrium, the surrounding β phase gradually transforms into α_{eq} or α_{lath}, causing precipitation and growth of a limited number of α_{fine}. Elevating the forging heating temperature results in an accumulation of strain in the early stages of forging, which in turn provides a driving force for subsequent heat treatment. This process promotes further growth of α_{fine}.

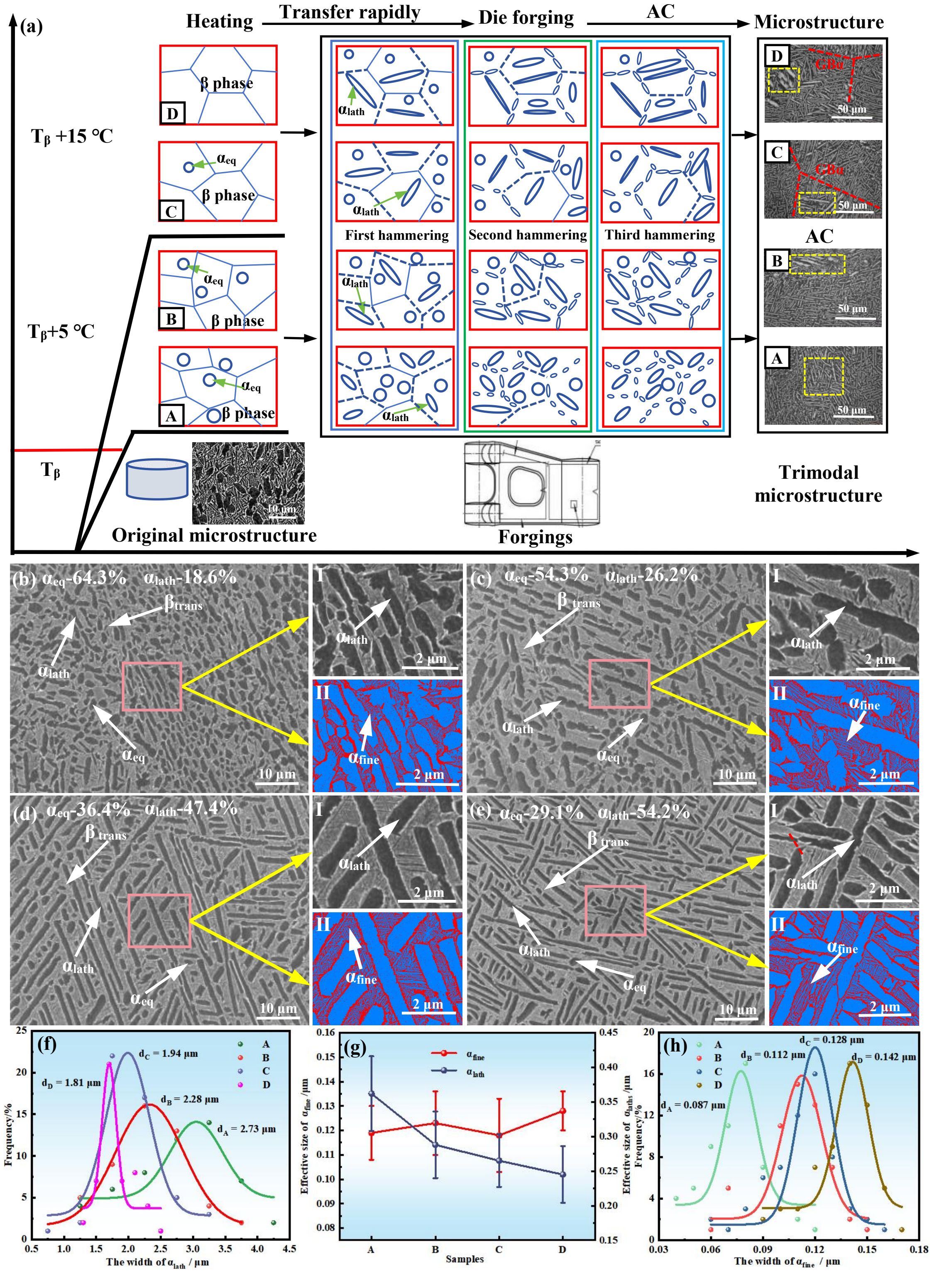

Fig. 3. (a) Microstructure evolution and characteristics of specimens A-D after quasi-β forging processes; (b-e) the microstructure after quasi-β forging and double heat treatment of specimens A-D; (f, h) the probability distributions are presented for the widths of α_{lath} and α_{fine} in specimens A-D; (g) the effective size of α_{lath} and α_{fine}.

3.2 Tensile properties

3.2.1 Tensile properties of TC21 forgings with distinct forging parameters

The stress-strain curves and the strength and plasticity variation after tensile testing are illustrated in Figs. 4a to 4b. It is clear that the tensile strength of TC21 forgings remains consistently around 1200 MPa, regardless of the quasi-β forging parameters used, with only a slight difference of 58 MPa between the maximum and minimum values. Additionally, there is minimal variation in post-break elongation, consistently exceeds 9%. As the forging heating temperature increases, both ultimate tensile and yield strength gradually rise, while plasticity decreases accordingly. Combined with the statistical analysis of microstructural parameters findings, a clear positive correlation is observed between strength and the α_{lath} content, while a negative correlation is found between strength and the α_{eq} content. Moreover, the plasticity index of TC21 forgings at lower forging heating temperature is higher than that of the high temperature. This can be attributed to the presence of a higher content of α_{eq} in the specimens A and B, along with a finer α_{fine}. The noteworthy aspect is that α_{fine} offers a large number of interfaces that impede the movement of dislocations, thereby contributing to some extent to the enhancement of intensity.

The study delves into a correlation between microstructural parameters and the tensile strength of TC21 forgings using the Hall-Petch formula[18, 19], as depicted in Figs. 4c to 4d. The primary objective is to elucidate the significant variation in strength resulting from the inconsistent microstructure of specimens under different forging parameters. With an increase in forging heating temperature, the strength increases with the decrease of $d\alpha_{lath}$ value (Fig. 4c). This phenomenon can be attributed to the increased α_{lath} content, which effectively impedes dislocation slip and crack propagation, thereby influencing the strength [26]. Additionally, an increase in the duration of forging holding time boosts nucleation driving force. While there is a rise in α_{lath} content is observed, leading to an augmentation in lath spacing. This phenomenon facilitates the growth of α_{fine} and β retained phase (β_r) within the β_{trans}, thereby diminishing the effect of α_{fine}/β_r interfacial strengthening (Fig. 4d). Consequently, this reduction in interface area promotes dislocation movement and slip, ultimately impacting material strength adversely [17]. The findings illustrated in Fig. 4a corroborate this trend, specifically highlighting that raising the forging heating temperature appropriately can result in a more flawless trimodal microstructure and significantly improve strength. Notably, the fitting coefficient of $d_{\alpha lath}$ to material strength surpasses that of $d\alpha_{fine}$, highlighting the predominant impact of α_{lath} on the strength over α_{fine} (Figs. 4c-4d).

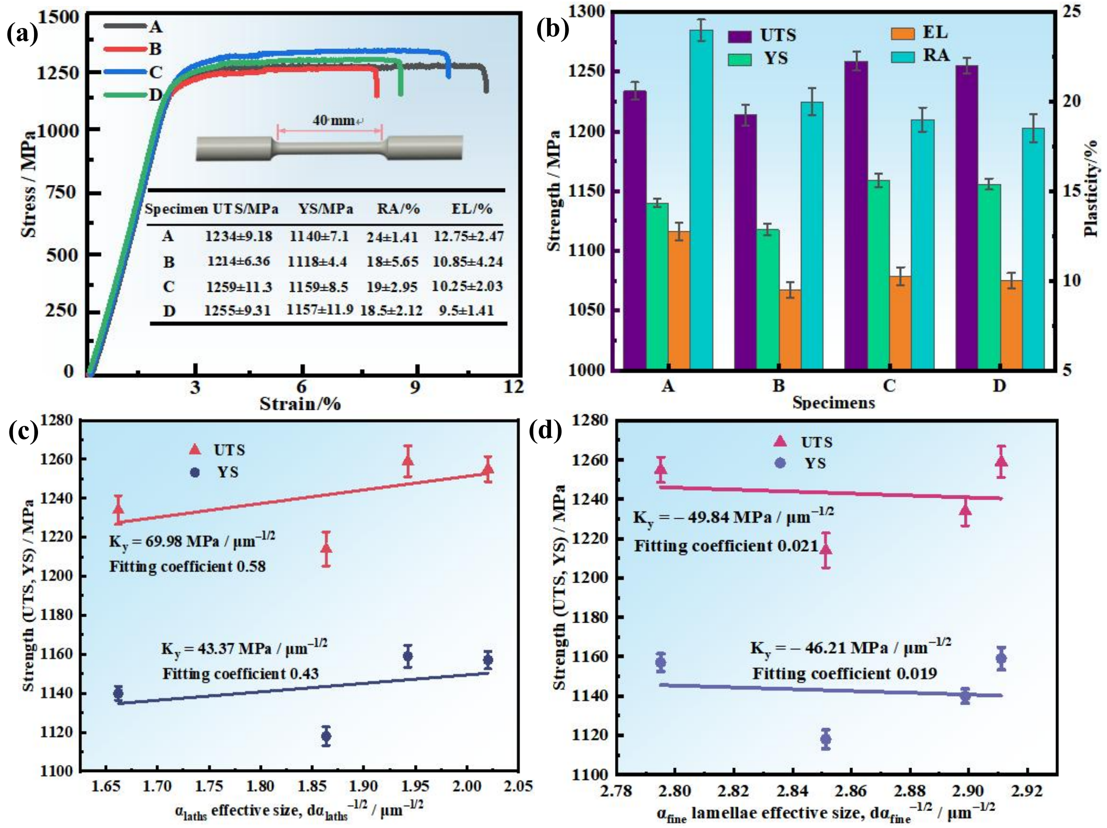

Fig. 4. Tensile properties under different forging parameters: (a) stress-strain curves, (b) yield strength (YS), ultimate tensile strength (UTS), elongation (El) and reduction of area (RA); (c-d) relationship between strength vs. reciprocal square root of α_{lath} effective size ($d\alpha_{lath}$) and α_{fine} effective size ($d\alpha_{fine}$).

3.2.2 Tensile fracture mechanism of TC21 forgings

Figs. 5A to 5D depict fracture morphological characteristics of tensile specimens post various forging conditions and heat treatments. Specifically, Figs. 5a to 5d present the tensile fracture morphology and micro image of fracture profiles, respectively. The fracture mechanism of the specimen encompasses a variety of fracture modes, included fractures induced by microvoids aggregation, brittle and cleavage fractures, as well as ductile fractures. The observed fracture features consist of dimples, tear ridges, cleavage planes, cleavage steps, and secondary cracks.

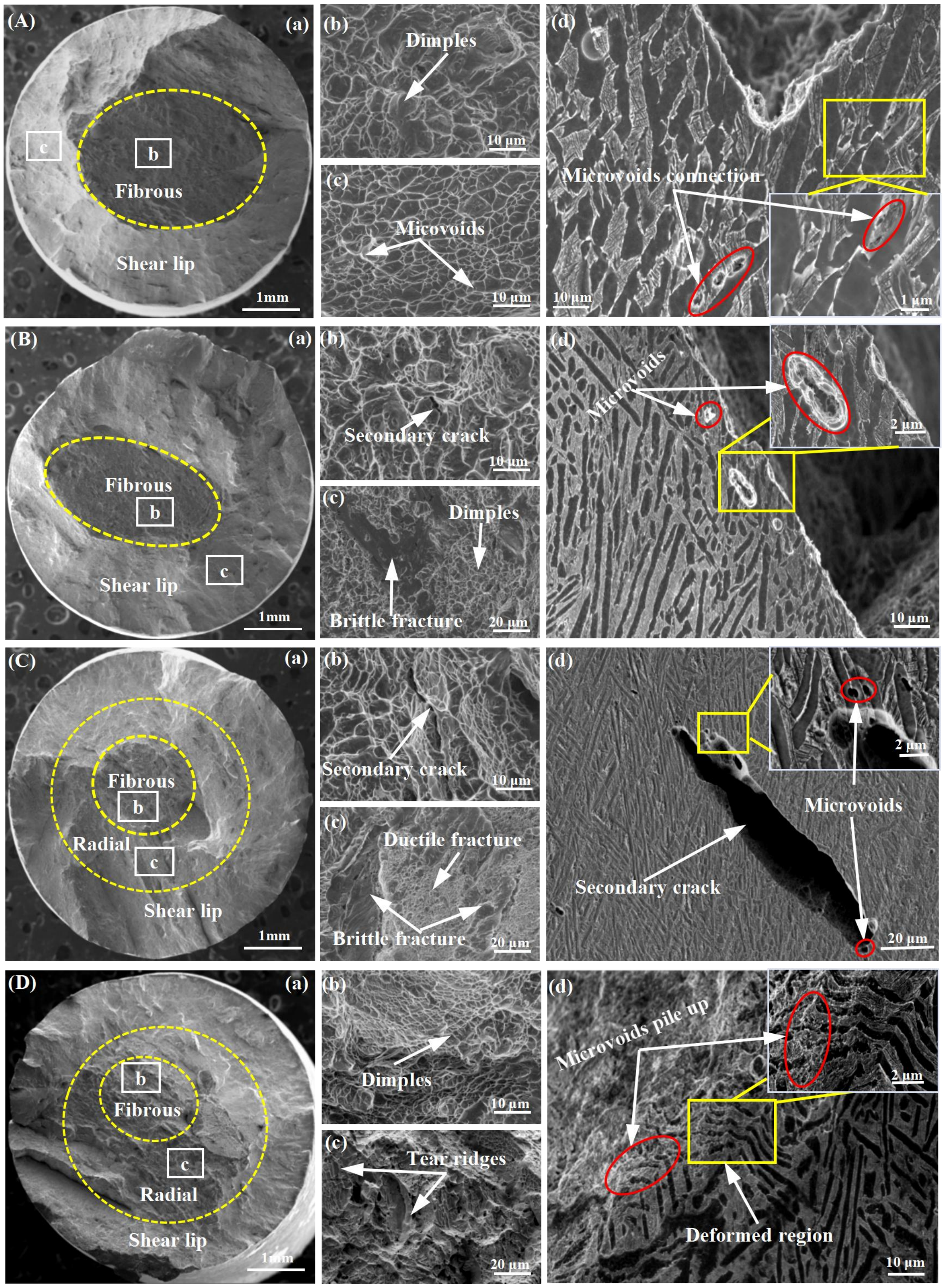

Fig. 5. Tensile fracture surfaces of TC21 forgings at different forging conditions: (A-D) specimens A-D; (a) low magnification of fracture, (b-c) micro image of fracture morphology; (d) micro image of fracture profiles.

Notably, the dimples exhibited a progressive decrease in size across the four specimens, with average diameters measuring 3.07, 2.79, 2.34, and 1.95 μm, respectively. The macroscopic fracture surfaces of specimens A and B display pronounced necking, resulting in a distinct flat step. Further analysis reveals that these fractures are primarily characterized by microvoids aggregation induced fractures, with a minor presence of cleavage fractures. In contrast, specimens C and D exhibit extensive cleavage facets and dimples are still visible but with smaller size, indicating that a mixed fracture mechanism plays a pivotal role during fracture process while the ductile fracture role is weakened. Cleavage facets corresponds to transgranular fractures with limited plasticity, while dimple regions indicates intergranular fractures with excellent plasticity [27]. Consequently, specimens with more dimples exhibit increased plasticity. The fracture profile indicates that the difference in strain at the $\alpha_{lath}/\beta_{trans}$ interfaces results in the formation of unevenly sized microvoids, which later combine and evolve into microcracks that propagate through or along the $\alpha_{lath}/\beta_{trans}$ interface, eventually forming into larger crack (Fig. 5d). Secondary cracks and deformation regions were observed near the crack propagation paths of specimens C and D, indicating inadequate coordinated deformation ability and limited plasticity.

3.3 Impact toughness

3.3.1 Impact performance of TC21 forgings with different forging parameters

The impact load-displacement curves of specimens under various forging conditions are depicted in Fig. 6a. The macroscopic curve displays the fitted data, while the experimental data is shown in the upper right corner. Fig. 6b illustrates the total impact fracture energy, while includes crack initiation energy (W_i), crack propagation energy (W_p), and shear lip formation energy (W_s) [28]. The integration of the fitting curve from the initial point to the maximum load represents W_i; W_p denotes the integration of the fitting curve from the maximum load to the turning point of subsequent load descent; and W_s indicates the integral of the fitting curve from the turning point of load to fracture. The sudden increase in stress induced by the impact pendulum drop triggers the formation of cracks, which subsequently undergoes rapid propagation leading to specimen fracture. Load-displacement curves reveal that the critical unstable loads for specimens A-D were determined to be 34.35, 35.04, 39.87, and 39.59 kN, respectively. The load then dropped linearly until the specimen broke. Statistical analysis of impact energies indicates that the majority of energy is consumed during the crack initiation stage, with values of 82.6, 76.2, 78.2, and 80% for specimens A-D, respectively.

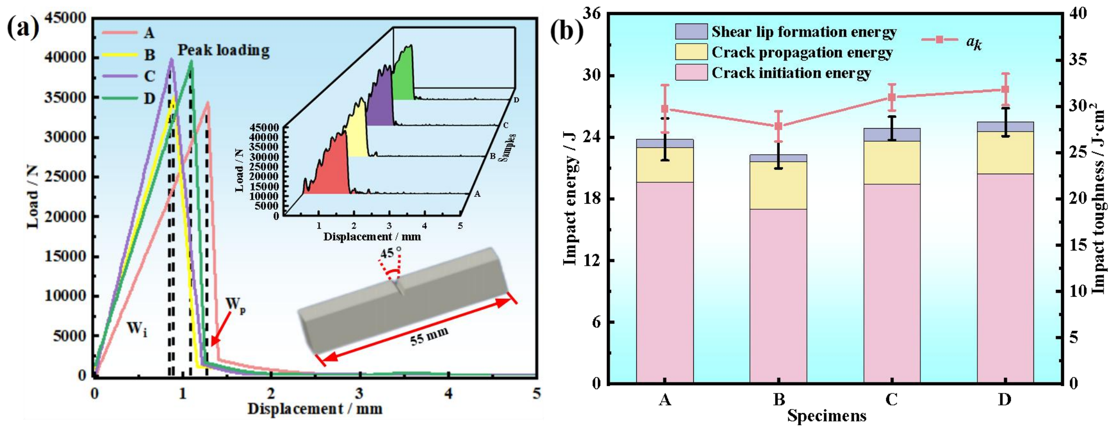

Fig. 6. (a) The impact load-displacement curves; (b) impact energy and a_k of specimens A-D.

3.3.2 Impact fracture morphology of TC21 forgings at varies forging parameters

To further investigate the different impact energies of specimens A-D, a comprehensive analysis of the impact fracture morphology was conducted, as illustrated in Fig. 7. The widths of crack initiation zone widths for specimens A-D are 0.575, 0.566, 0.605, and 0.614 mm, respectively (Figs. 7b, 7e, 7h and 7k). A noticeable correlation was observed between the width of the crack initiation zone and the corresponding crack initiation energies. This suggests that specimens C and D exhibited relatively limited capabilities to coordinate plastic deformation, leading to a continuous and rough fracture surface with an abundance of larger secondary cracks, 'river-like' cleavage facets, and tear ridges within the crack propagation zone (Figs. 7h and 7k).

In contrast, specimens A and B displayed smaller secondary cracks in the crack initiation region, coupled with a higher content of dimples in the crack propagation region and fewer cleavage facets (Figs. 7b and 7e). In contrast to specimen A, a limited number of secondary cracks were observed within the crack propagation zone of specimen B. Moreover, specimens C and D exhibited tear ridges and cleavage fractures during crack propagation, contributing to a rougher fracture surface (Figs. 7i and 7l). Interestingly, the tear ridges in specimen D appeared sharper and covered a larger area compared to those in specimen C. However, tearing ridges and cleavage facets required less energy compared to dimple formation , resulting in slightly lower crack propagation energy. While both crack initiation energy and crack propagation energy influence the overall impact energy to some extent, it is crucial to highlight that impact energy is more significantly influenced by the former.

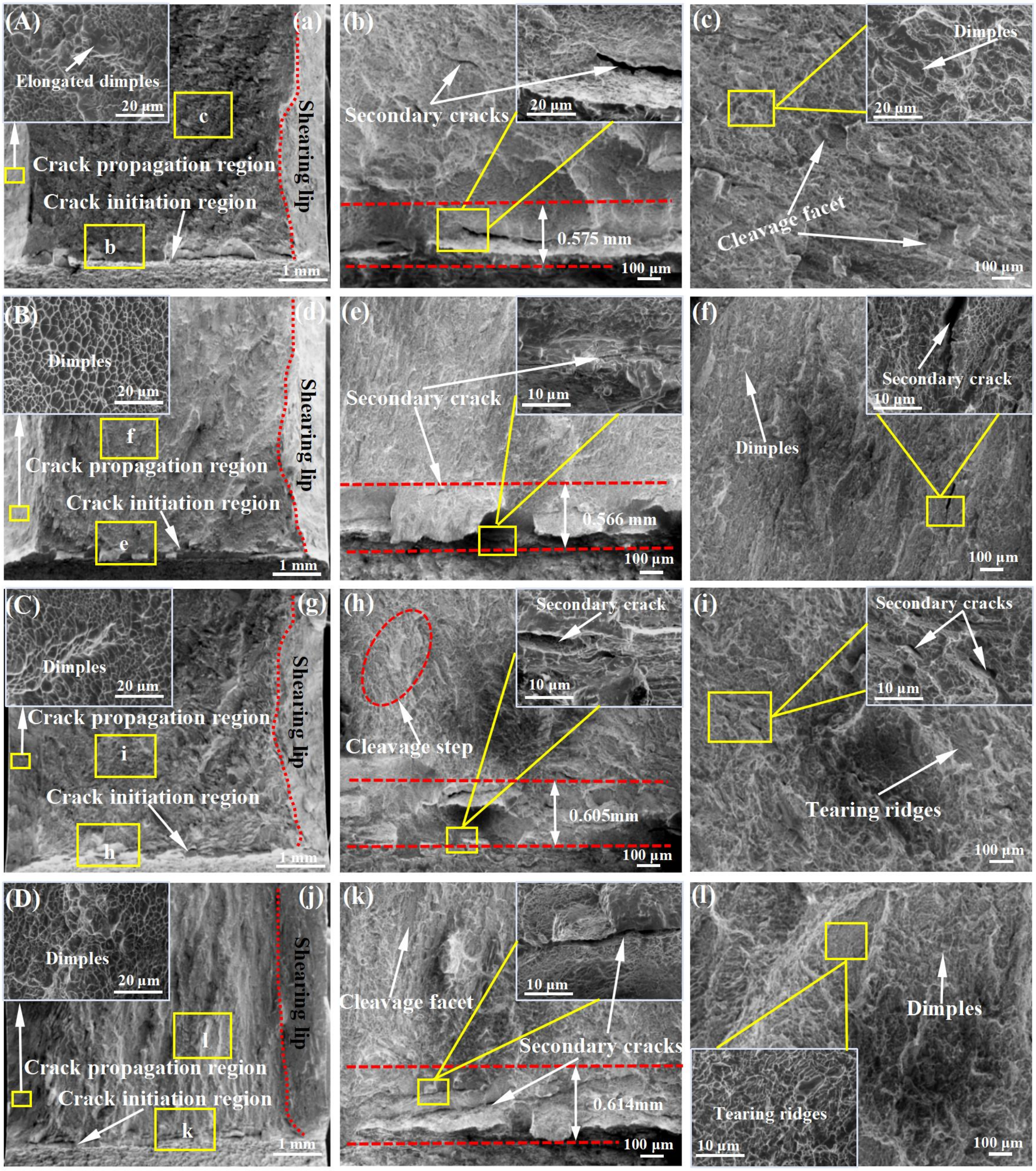

Fig. 7. Fracture morphology after impact tests of specimens A-D; (a), (d), (g) and (j) macroscopic fracture surface morphology; (b), (e), (h) and (k) secondary cracks in macroscopic crack initiation region; (d) macroscopic crack propagation region; (c), (f), (i) and (l) crack propagation region showing dimples, tearing ridges, or cleavage facets.

3.3.3 Crack propagation path of TC21 forgings at distinct forging parameters

The macroscopic and localized microscopic morphology of crack propagation paths for specimens A-D is illustrated in Fig. 8. Figs. 8A to 8D display the macroscopic fracture profiles of specimens A-D, and crack propagation direction from left to right. Distinct undulations are visible in the crack initiation area near the notch root region, attributed to the presence of secondary cracks (Figs. 8a, 8d, 8g, 8j). It is important to highlight that there are variations in the crack propagation patterns among specimens, with specimens C and D showing higher levels of undulation compared to specimens A and B. This behavior can be explained by cleavage facet formation resulting from non-coordinated deformation between tear ridges and microstructure under shear stress, as supported by observations on the fracture surfaces in Fig. 7i and Fig. 7l.

Specimens A and B primarily demonstrate fracture mechanisms caused by the aggregation of microvoids and cracks propagation along the $\alpha_{eq}/\beta_{trans}$ interface (Figs. 8a to 8f). However, the presence of α_{eq} in the microstructure hinders crack propagation paths along the $\alpha_{eq}/\beta_{trans}$ interface, leading to rougher microscopic crack propagation paths. Specimens C and D primarily showcase microvoids aggregation-induced fracture, cracks propagation along the $\alpha_{lath}/\beta_{trans}$ interface, and cracks propagation through the α_{lath}. The increased content of α_{lath} hinders microstructure deformation coordination, leading to the aggregation and interconnection of microvoids while intensifying microstructural deformations near the crack propagation zone. Observations revealed significant slip lines, torsional deformations, and shear fractures in the α_{lath}, highlighting its susceptibility to plastic deformation (Figs. 8h to 8l). The frequency of crack deflection decreases at higher forging heating temperatures (Figs. 8C and D) possibly due to the longer propagation path of cracks along the $\alpha_{lath}/\beta_{trans}$ interface compared to that along the $\alpha_{eq}/\beta_{trans}$ interface. This may also result in cleavage fracture or the formation of a flat path by shearing the thinner α_{lath}, thereby impeding improvement in impact crack propagation energy.

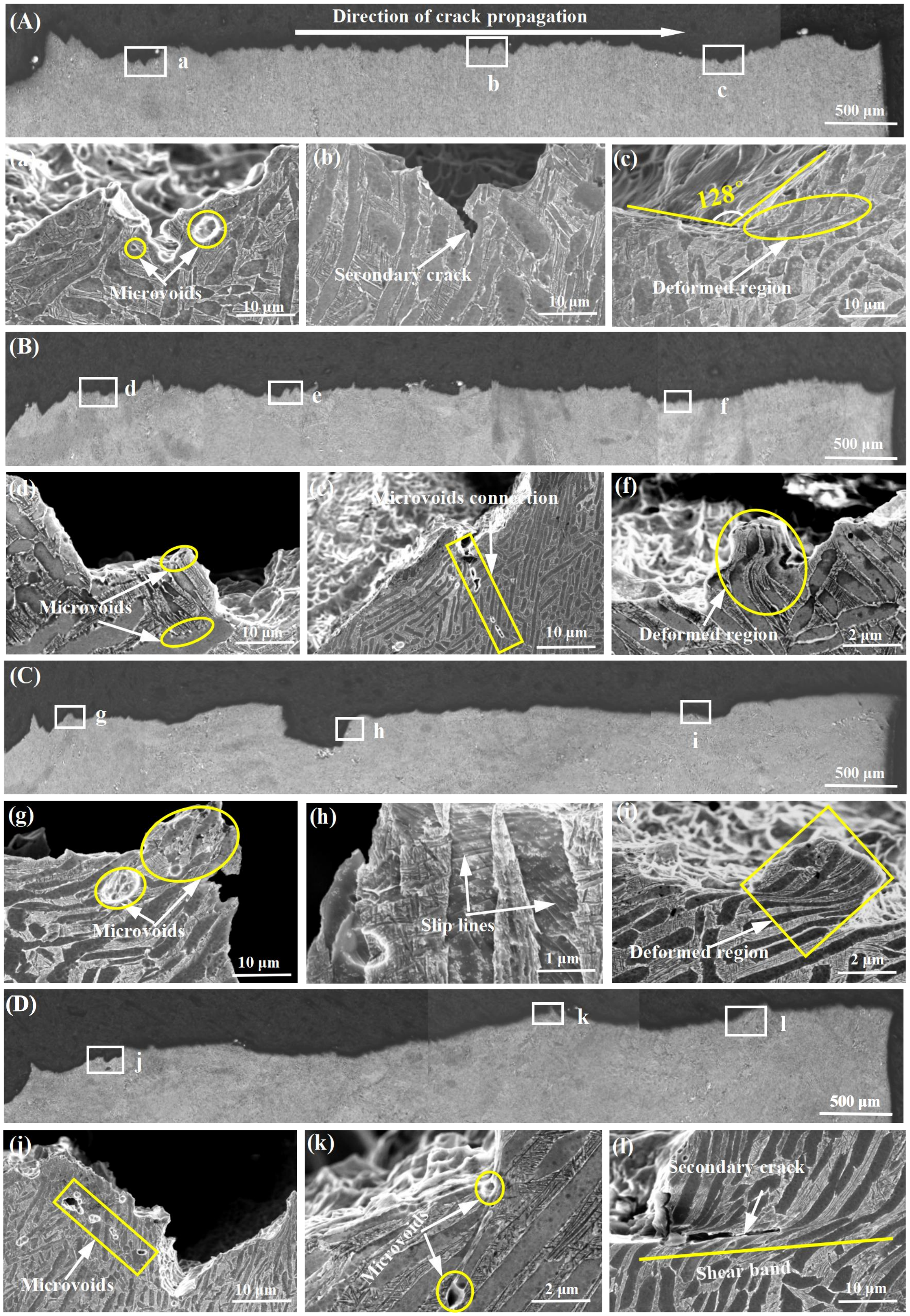

Fig. 8. Impact fracture profile of TC21 forgings with different forging parameters: (A-D) specimens A-D; (a), (d), (g) and (j) microvoids at the crack initiation region; (b), (e), (h) and (k) microcrack or slip lines at the crack propagation region; (c), (f) , (i) and (l) microstructural deformation or shear bands at the crack propagation stage.

3.3.4 Impact fracture mechanism and dislocation evolution of TC21 forgings

The microstructural deformation characteristics below the crack initiation stage in the impact specimens under different forging parameters are depicted in Fig. 9. In specimen A, exhibiting superior coordinated plastic deformation due to a higher content of α_{eq}, dislocation accumulation is minimized, thus delaying stress concentration at the interface. Furthermore, the smaller size of α_{fine} implies a greater number of phase interfaces that impede dislocation slip and effectively boost local resistance against crack initiation. This is supported by the significant dislocation entanglement and stacking faults observed in α_{fine}, as well as twins that help alleviate stress concentration (Figs. 9a to 9c). Similarly, dislocations accumulate at the $\alpha_{lath}/\beta_{trans}$ interface in specimen B and progressively propagate into the interior of α_{lath} to form crossed dislocation slip lines at an angle of approximately 60°. Some slip bands are confined within α_{eq}, which moderately hinder crack propagation (Figs. 9d- to 9f). Based on the aforementioned results, it can be deduced that compared to α_{eq}, impact damage is more prone to occur in α_{lath}.

In specimen C, a few flat slip bands traverse the α_{lath}, and slip lines are detected within some α_{lath}, with a pinch angle of approximately 68°, while is greater than that in specimen B (Figs. 9e and 9g). A small angle between dislocation lines restricts their slip path due to constraints from the crystal structure, thereby impeding their movement. The limited angle hinders dislocations from finding suitable planes and directions for sliding within the crystal, consequently inhibiting their sliding behavior [7, 29]. The α_{lath} with small thickness in specimen D facilitates the accumulation of dislocations at the $\alpha_{lath}/\beta_{trans}$ interface. This exacerbates the plastic deformation induced by local stress concentration, ultimately leading to shear fracture of the α_{lath} under stress (Figs. 9g and 9k). Similarly, some α_{fine} particles are sheared into nanoparticles, effectively absorbing impact energy. In summary, the α_{eq} exhibits superior deformation coordination and longer dislocation slip distances, effectively impeding crack propagation within α_{eq} phase while facilitating crack propagation along the phase interface [16]. In contrast, the α_{lath} is highly susceptible to shear forces from impact loading, resulting in crack initiation and specimens rapid fracture, which consumes a considerable amount of impact energy. The plastic deformation behavior and dislocation hindering capacity of α_{fine} particles vary depending on their size. With increasing size, these particles experience dislocations tangles (Fig. 9c), stacking faults (Fig. 9i), and shear fractures (Fig. 9l) in sequence. This observation indicates that both α_{lath} and larger α_{fine} particles are more prone to initiating fracture events that consume a significant amount of energy for crack initiation.

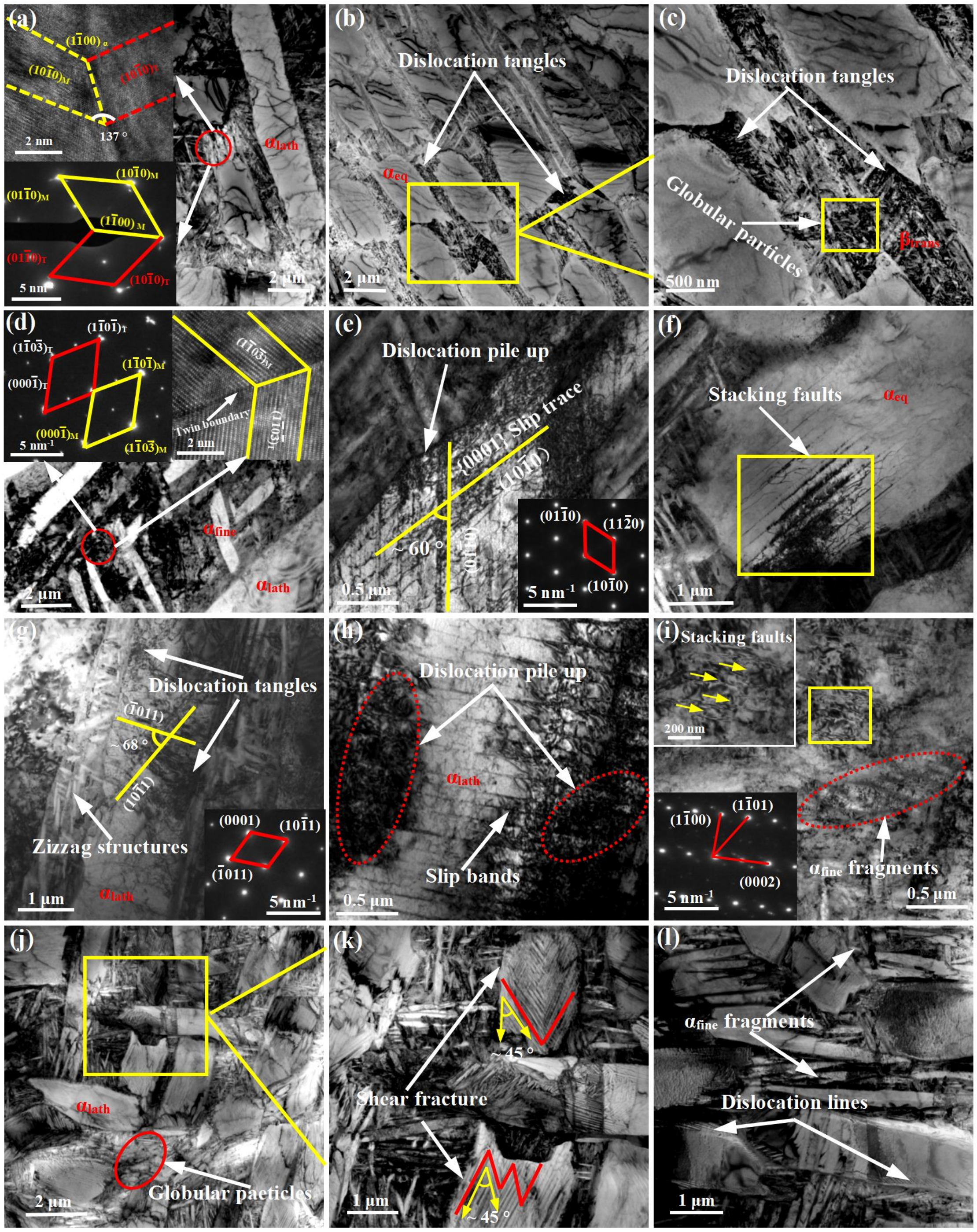

Fig. 9. Dislocation structures of crack initiation regions of impact specimens A (a-c), B (d-f); C (g-i) and D (j-l); (a-c) high density of dislocation and twin in α_{fine}; (d-f) a few twin emerged from α_{fine}, observed as intersections of dislocation lines and stacking faults within the $\alpha_{lath;}$ (g-i) the interaction between dislocations and slip bands at the $\alpha_{lath}/\beta_{trans}$ interface enhances deformation, with partially deformed α_{fine} with stacking faults; (j-l) the α_{lath} and α_{fine} experience the maximum shear stress, which leads to their fragmentation under the influence of shearing forces.

3.4 Fracture toughness

3.4.1 Fracture toughness of TC21 forgings with different forging parameters

The load-displacement and toughness variation curves of CT specimens under different forging parameters are shown in Fig. 10a. The maximum load values, which indicate crack destabilization strengths, were 47.73, 44.81, 45.68, and 47.97 kN, respectively. It was found from load-displacement curves that the cracks absorbed energies of 62.9, 51.1, 53.5, and 67.3 J, respectively. A higher maximum load value suggests better fracture resistance of the material being tested, aligning with the trends observed in energy absorption. At elevated forging heating temperatures, both a_k and K_{IC} values show an increase compared to lower forging heating temperatures, with an average improvement of 9.4% for a_k and 0.15% for K_{IC}. It is noteworthy that the K_{IC} values for all specimens were observed to exceed 80 MPa·m$^{1/2}$.

Previous studies have established a correlation between K_{IC} and the tortuosity of crack propagation paths, as well as the size of the plastic deformation zone at the crack tip [30]. Some researchers contended that a more tortuous crack propagation path and a wider plastic deformation area at the crack tip result in greater consumption of crack propagation work and improved K_{IC} [31]. LSCM was employed in this research to examine the fracture morphology of CT specimens subjected to four distinct forging parameters (Figs. 10c to 10f). The aim was to evaluate the influence of the surface roughness (S_a) and the ratio of fracture surface area (A_{real}/A_{macro}) on K_{IC} [19]. The S_a on fracture surfaces and the projected area (A_{macro}) decrease as the true area (A_{real}) increases, thereby leading to a consistent trend for A_{real}/A_{macro} and S_a (Fig. 10b). However, it is noteworthy that under specimen A forging conditions, both A_{real}/A_{macro} and S_a values are larger compared to those under specimen D. Surprisingly, the K_{IC} value for the specimen A (80.4 MPa·m$^{1/2}$) is lightly smaller than that for the specimen D (81.35 MPa·m$^{1/2}$). This suggests that while the degree of tortuous in the crack propagation path and its roughness play an important role in determining the K_{IC} value, they are not the sole determining factors.

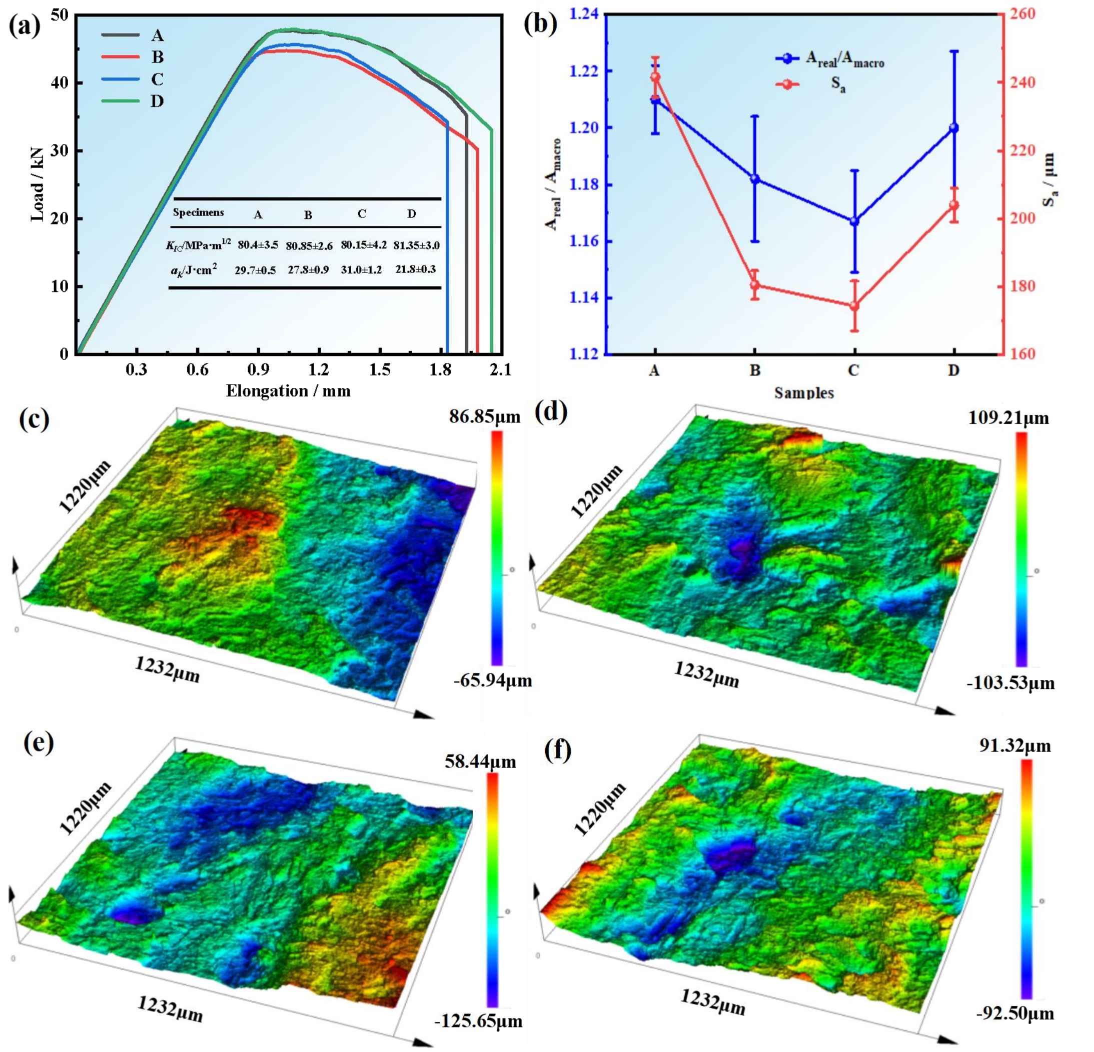

Fig. 10. (a) Displacement-load curves of CT specimens and the changing trend of a_k and K_{IC} at different forging parameters; (b) statistical charts of surface area ratio and surface roughness; (c-f) LSCM fracture morphology of specimens A-D.

3.4.2 Fracture morphology of TC21 forgings with different forging parameters

Fig. 11 was utilized to analyze the fracture morphology of CT specimens to gain a deeper understanding of the aforementioned phenomenon. The fracture surface was divided into two main regions: the fatigue prefabricated crack region and the crack propagation region (Figs. 11a to 11j). The prefabricated crack region exhibited a smooth surface, while the propagation region displayed roughness with a distinct interface between the two regions. The presence of fatigue striations and secondary cracks in the prefabricated crack region was attributed to minor plastic deformation and fatigue damage in stress concentration areas during cyclic loading [32].

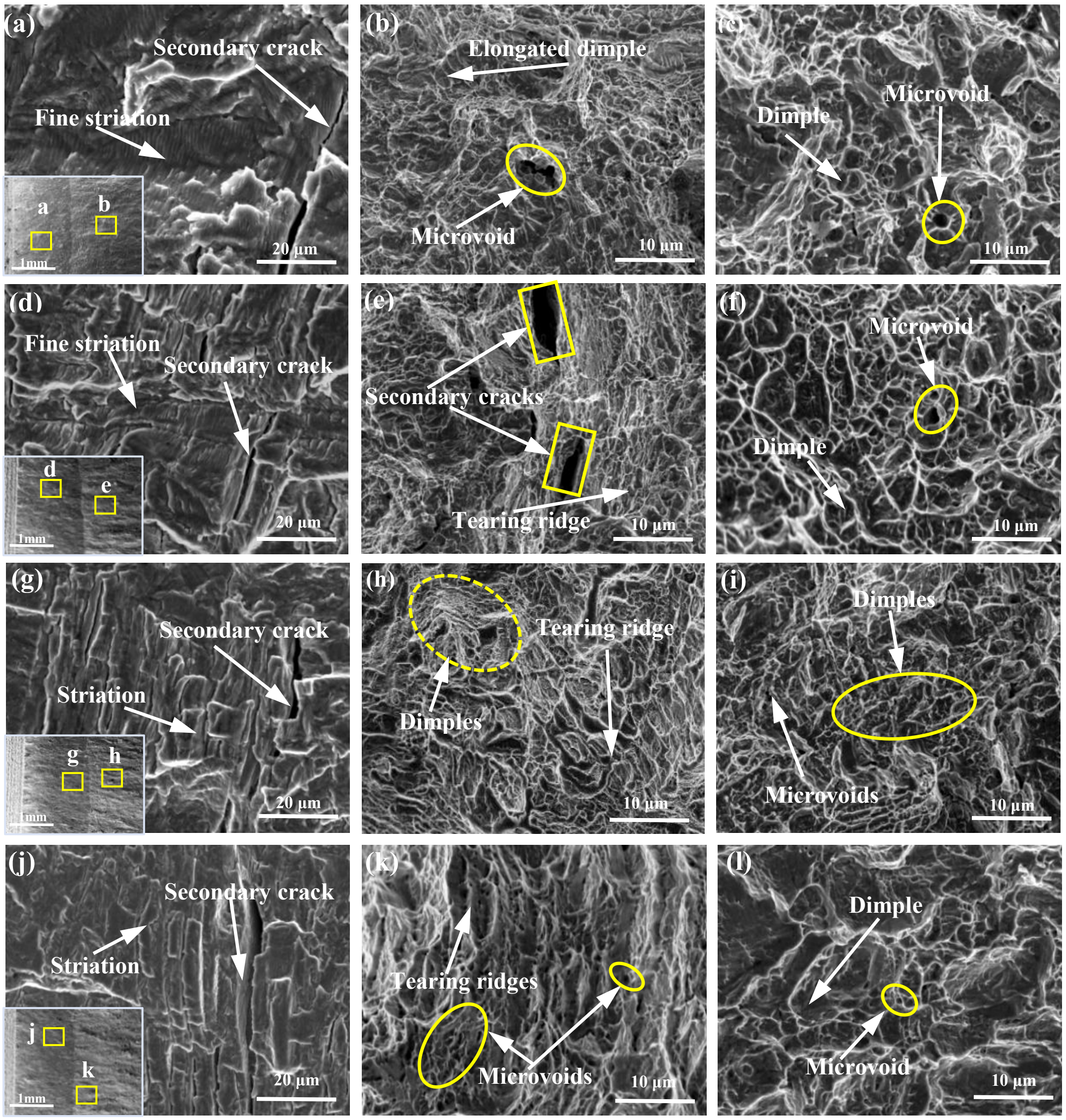

Fig. 11. Fracture morphology of CT specimens at different forging parameters: (a-c) specimen A; (d-f) specimen B; (g-i) specimen C; (j-l) specimen D; (a), (d) , (g) and (j) macroscopic fatigue striations and secondary cracks at the fatigue prefabricated crack region; (b), (e) , (h) and (k) cleavage facet, dimples, tearing ridges or secondary cracks appear at the crack propagation region; (c), (f), (i) and (l) dimples and microvoids characteristics.

Moreover, the fracture surfaces of specimens A and B display numerous distinct dimples and a few microvoids, which are characteristic of ductile fracture (Figs. 11a to 11f). Conversely, specimens C and D show tear ridges surrounded by dimples, indicating a mixed fracture mode (Figs. 11g to 11l). These tear ridges hinder crack propagation by providing additional resistance, thus consuming a amounts of crack propagation energy. Prior research has demonstrated that tear ridges form due to α phase detachment under stress. This study corroborates this phenomenon and establishes a noteworthy association. The α_{lath} displays larger dimensions at elevated forging heating temperatures, resulting in the creation of more uniform and well-defined protrusions on the tear ridge. The presence of tear ridges, coupled with deeper microvoids, signifies an improved capacity for plastic deformation, thereby diminishing stress concentration at crack tips and augmenting the energy required for crack propagation.

3.4.3 Crack propagation paths of CT specimens

The distribution of long crack propagation paths in CT specimens under different forging parameters is depicted in Figs. 12A and 12D. The macroscopic propagation directions of the cracks is from left to right. As shown in the Figs. 12A to 12B, the long crack propagation path of specimens A and B is relatively flat with fewer undulations. Furthermore, the microvoids of specimens A and B initiated at the α_{eq}/β_{lath} interface but remained unconnected, exhibiting minimal microstructural deformation near the crack propagation path (Figs. 12a to 12f). This behavior can be attributed to the coordinated deformation of a significant number of α_{eq}, which effectively mitigated stress concentration.

In contrast, specimens C and D exhibit increased fluctuations in their fracture surfaces with a higher frequency of crack deflection and more noticeable plastic deformation of the local microstructure (Figs. 12g to 12l). Meanwhile, it also indicates that the ability of α_{lath} to impede crack propagation is much higher than α_{eq}. Additionally, a considerable number of microvoids and microcracks emerge and interconnect at the $\alpha_{lath}/\beta_{trans}$ interface and within α_{lath}, which facilitates the plastic deformation of the microstructure near the crack tip. Further detailed observations revealed inconsistent morphology characteristics in secondary cracks near the crack propagation in four specimens. Specimens A and B exhibited smaller secondary crack sizes and experienced slight deflection during propagation, suggesting superior coordination in deformation. In contrast, samples C and D exhibit larger dimensions and deflection in their secondary cracks, as well as larger regions of plastic deformation at the crack tip (Figs. 12c, 12f, 12i and 12l). The findings indicate that the α_{eq} exhibits greater resistance to fracture and deformation compared to the α_{lath}. Moreover, the frequency of crack deflection and the extent of plastic deformation at the secondary crack tip increase proportionally with the size of the α_{fine}.

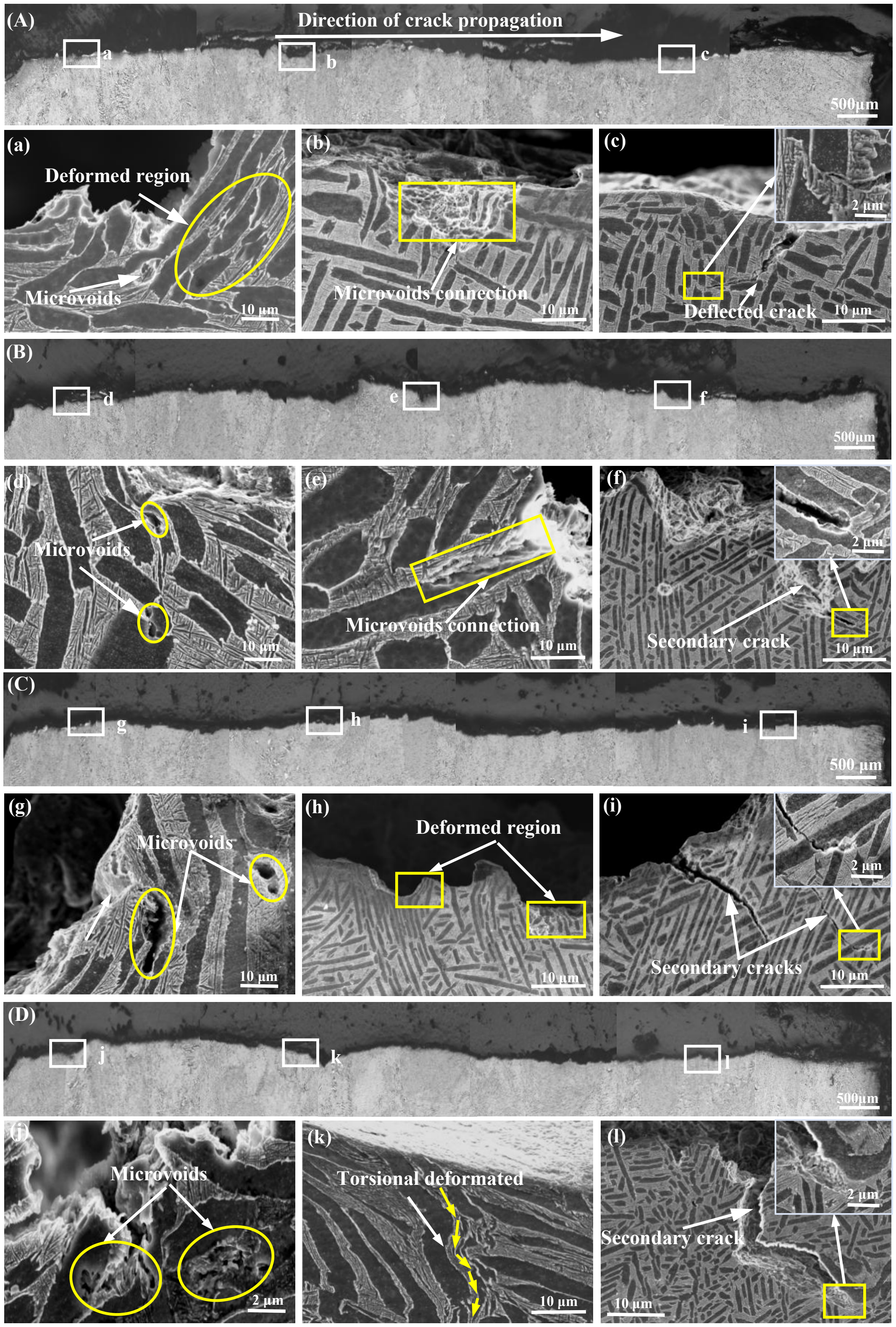

Fig. 12. Fracture profile of CT specimens at different forging parameters: (a-c) specimen A; (d-f) specimen B; (g-h) specimen C; (j-l) specimen D; (A) - (D) macroscopic fracture profile; (a), (d), (g) and (j) microvoids and deformed regions were observed near the crack initiation region; (b), (e), (h) and (k) microvoids and microstructural deformation in the crack propagation region; (c), (f), (i) and (l) plastic deformation zone at the secondary crack tip.

4. Discussions

4.1 Effect of forging parameters on microstructure of TC21 forgings

The variations in forging parameters introduce significant inconsistencies in the microstructural characterization after heat treatment [33]. Under identical initial forging heating temperature conditions, both specimens A and B exhibit similar driving forces for the phase transition. Increasing the duration of the forging heating holding time not only facilitates the conversion of the α phase to the β phase and enhances the Gibbs free energy of the β phase [5]. It also ensuring that the alloy maintains a stable temperature close to the phase transition point, thereby promoting the phase change process. Subsequent cooling of the alloy below the phase transition point leads to atom rearrangement within the solid solution, facilitating precipitation and coarsening of both α_{eq} and a minor amount of α_{lath}. During die forging, deformation forces cause a portion of α_{eq} to transform into α_{lath}. Consequently, there is an increase in content for α_{lath} while a decrease in content for α_{eq}. This trend becomes more pronounced with longer forging heating holding times.

Moreover, during forging processes near the β_{trans} temperature (T_β + 5 °C), where higher grain boundary energies prevail, grains tend to form equiaxial microstructure with smaller surface area and lower energy. As a result, some α_{eq} is retained within the trimodal microstructure. Consequently, there was a decrease in the α_{eq} content of specimen B to approximately 54.3%, along with an increase in the α_{lath} content to around 26.2% (Fig. 3). As the temperature of the forging heating increases (T_β + 15 °C), a significant portion of the original α phase undergoes a phase transition to the β phase, resulting in an increase in the Gibbs free energy of the β phase. Subsequent forging and AC lead to preferential precipitation of numerous α_{eq} phases from the β phase, forming the α_{lath} under deformation forces. Furthermore, phase diffusion between the original β phase and newly formed α phase intensifies. The freshly generated α phase diffuses along the grain boundaries of the original β phase, further promoting the formation of α_{lath} [19]. Notably, a higher forging temperature leads to greater strain accumulation during initial forging, providing impetus for subsequent heat treatment to induce precipitation of α_{fine}. As stored energy from early deformation diminishes with heat treatment, the β phase gradually does not precipitate the α_{fine}, while coarsening of α_{fine} assumes a more prominent role.

4.2 Effect of forging parameters on strength of TC21 forgings

It is widely recognized that the α/β interface impedes dislocation motion, thereby influencing material strength to a certain degree [34, 35]. Nevertheless, variations in microstructure can lead to inconsistencies in the α/β interface region, particularly in the context of the trimodal microstructure. Previous studies have not extensively investigated the relative significance of different microstructural parameters that influence mechanical properties of TC21 forgings, which creates uncertainty regarding the main parameters that predominantly affect these properties [36]. The Hall-Petch formula not only establishes a relationship between microstructural parameters and mechanical properties but also offers compelling evidence for the correlation between mechanical properties and microstructure [14, 18]. In the present study, the Hall-Petch formula fitting coefficient of $d\alpha_{lath}$ to material strength surpasses that of $d\alpha_{fine}$, highlighting the predominant impact of α_{lath} on the strength over α_{fine}. The microstructures of specimens forged at high temperatures displayed higher contents of α_{lath}, resulting in superior strength compared to those forged at lower temperatures. The strength increases by 23 MPa and 41 MPa, respectively, when compared with the lower forging heating temperatures (Figs. 4a and 4b). A more comprehensive analysis demonstrates that an increase in forging heating temperature leads to a decrease in the effective size of α_{lath}, resulting in wider spacing between plates. This enhances uniformity and improves the ability to impede dislocation slip within the intricately interwoven α_{lath}. Moreover, the increased plate spacing facilitates the growth of α_{fine} within the β_{trans} matrix, thereby reducing hindrance caused by α_{fine}/β_r interfaces on dislocations while simultaneously intensifying interactions at $\alpha_{lath}/\beta_{trans}$ interfaces. Consequently, the strength is effectively enhanced. Notably, extending the forging holding time results in a slight decrease in strength. This can be attributed to the reduction in the α_{fine}/β_r interface due to the increase in α_{fine} size, which is unfavorable to strength. Furthermore, the most significant strength fluctuation was observed when the α_{lath} content in the microstructure is minimal, indicating a strong correlation between the strength and the α_{lath}.

4.3 Effect of forging parameters on plasticity of TC21 forgings

The tensile fracture reveals that the area of cleavages facets and tear ridges with low plasticity rises, while the area of dimples with high plasticity decreases as the forging heating temperature increases (Fig. 5). Dimples consume much more plastic deformation energy than cleavage facets and tear ridges, which implies that lower forging heating temperatures result in a superior plasticity, as supported by the data presented in Fig. 4. The analysis of microstructure evolution reveals a positive correlation between plasticity and the volume fraction of α_{eq}, while an inverse relationship exists with the volume fraction of α_{lath} (Fig. 3). Increasing the forging heating temperature leads to a decrease in plasticity alongside a reduction in the volume fraction of α_{eq}. This suggests that α_{eq} has a more significant impact on plasticity compared to α_{lath}. These findings are consistent with previous research [37, 38, 39], highlighting the dominant influence of α_{eq} on plasticity.

Furthermore, the grain orientation of α_{eq} with a smaller aspect ratio is randomly distributed, thereby activating multiple sliding systems and increasing the distance over which dislocation slips occur [16]. This ability to undergo slip facilitates adaptation to external stresses and enhances coordination in plastic deformation. In contrast, α_{lath} with a larger aspect ratio exhibits limited deformation coordination capability during tensile fracture, reducing damage resistance. Consequently, the $\alpha_{lath}/\beta_{trans}$ interface acts as a stress concentration weak point that intensifies localized plastic deformation and promotes crack initiation, resulting in more cleavage facets and tear ridges typical of brittle fracture. Moreover, lower forging heating temperatures promote the presence of smaller α_{fine} in the microstructure, facilitating coordinated deformation and enhancing plasticity. However, due to its limited quantity compared to α_{eq}, the influence of α_{fine} on plasticity is considered insignificant. As the forging heating temperature increases, plasticity decreases along with a reduction in the ratio of α_{eq}. This underscores the greater significance of α_{eq} over α_{lath} and α_{fine} in determining the plasticity of TC21 forgings.

4.4 Effect of forging parameters on toughness of TC21 forgings

Previous studies have indicated that refining α_{fine} and increasing the proportion of α_{lath} and α_{eq} can improve the toughness of titanium alloy [40]. Specifically, a smaller size of α_{eq} within the microstructure leads to a wider dislocation slip free range, promoting the generation of multi-system slip, which helps in strain release and delays crack initiation [41]. Moreover, cracks are more likely to bypass α_{eq} with a shorter path due to its smaller aspect ratio. In contrast, α_{lath} has a lower slip free range and is more susceptible to localized plastic strain, which exacerbates the formation of microvoids and microcracks [42]. This observation is consistent with our impact fracture analysis, which indicates a reduced crack initiation zone area at lower forging heating temperatures. This effect is attributed to a higher α_{eq} content, which effectively inhibits crack initiation as illustrated in Fig. 7. In contrast, α_{lath} displays heightened susceptibility to dislocation accumulation at the interface under external loads, ultimately leading to substantial shear fracture. While this demands substantial energy for crack initiation, it also accelerates premature specimen fracture (Fig. 9). Furthermore, the higher aspect ratio of α_{lath} necessitates longer crack paths for propagation, thereby improving its resistance to crack propagation compared to α_{eq}. Reducing the α_{fine} size improves resistance to crack initiation by increasing the number of interfaces that impede dislocation slip. Under impact conditions, twins in α_{fine} effectively mitigate and distribute stress [18]. Further analysis reveals that enlarging α_{fine} size leads to increased atomic spacing, dislocation, and total strain in twins (Figs. 13a-13j). This is linked to reduced grain boundary area and heightened dislocation density in grains due to larger α_{fine} dimensions. Consequently, the formation and alteration of twin interfaces could trigger crack formation and the onset of fracture. Furthermore, the presence of α_{fine} alters the direction of crack propagation, leading to a greater consumption of energy for crack propagation. The coordinated deformation and fracture of both α_{lath} and α_{fine} intensify the consumption of impact crack initiation energy compared to α_{eq}, significantly influencing overall impact energy.

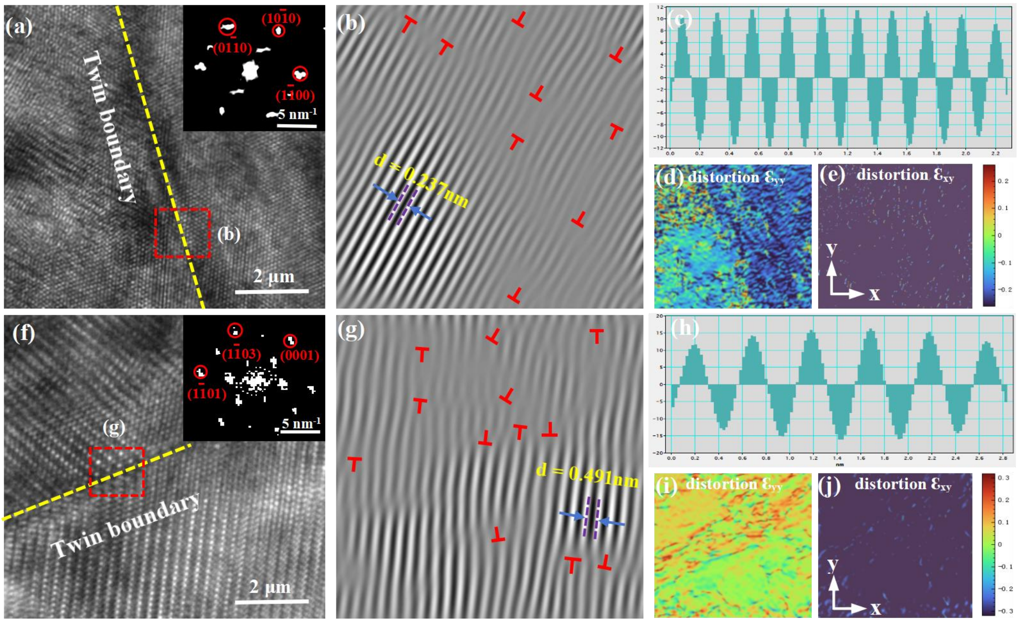

Fig. 13. (a) and (f) High resolution (HR) TEM and fast fourier transform (FFT) spot images of twins within the α_{fine} in specimens A and B; (b) ,(c), (g) and (h) inverse FFT patterns and atoms spacing of (a) and (f); (d-e) and (i-j) geometric phase analysis (GPA) of (a) and (f).

To investigate the disparity in K_{IC} resulting from microstructural variations induced by different forging parameters, we analyzed the fracture morphology of specimens A and D during crack propagation rate (*da/dN*) testing, as illustrated in Fig. 14. Two distinct modes of crack propagation were identified on the fracture surfaces of these specimens, as depicted in Figs. 14a to 14b. The dimensions of crack propagation regions I and II in specimens A and D were measured using IPP 8.0 software, as documented in Table 2. The equivalent radii (*R*) of the areas projected onto the plane perpendicular to the maximum principal stress are denoted as R_I and R_{II}, respectively. It is widely recognized that metals with high K_{IC} typically exhibit superior fatigue resistance [43]. The stress intensity factors (ΔK) at the tips of zones I and II were calculated using the equation [44, 45], $\Delta K = \frac{2}{\pi} \times \Delta\sigma \times \sqrt{\pi \times \mathrm{R}}$, where $\Delta\sigma$ represents the stress range. Subsequently, based on the concept of linear elastic fracture mechanics, the ASTM E647 standard provides an analytical expression for the stress field strength factor [46]:

$$K = \frac{P}{B \times \sqrt{W}} \times \frac{2+\alpha}{(1-\alpha)^{\frac{3}{2}}}(0.866 + 4.64\alpha - 13.32\alpha^2 + 14.72\alpha^3 - 5.6\alpha^4)$$

where α=a/W, P is the applied load. The formula mentioned above is valid when P is equal to either the maximum or minimum load value (with K being either K_{max} or K_{min}). It is crucial to emphasize that this formula is applicable only when α is greater than or equal to 0.2. In our study, however, the α value varies between 0.33 and 0.67. ABAQUS software was used to simulate the crack propagation paths of specimens A and D under varying ΔK. The results reveal a notable disparity in stress levels at the crack tip between specimens D and A (Figs. 14 b and 14e). The difference in fracture behavior between specimen A and specimen D can be attributed to the higher α_{eq} content in specimen A (Fig. 11). This higher content helps to reduce stress concentration at the crack tip, resulting in a longer and faster crack propagation process compared to specimen D. In specimen D, the crack propagation accelerated as it moves from the interface of α_{lath} with a large grain size into the next grain.

Table 2. Projection area and equivalent radius of the fracture surface after the K_{IC} test

Specimens	S_I / m^2	S_{II} / m^2	R_I / m	R_{II} / m
A	2.25×10^{-4}	4.5×10^{-4}	0.845×10^{-2}	1.197×10^{-2}
D	4.875×10^{-4}	1.875×10^{-4}	1.246×10^{-2}	0.773×10^{-2}

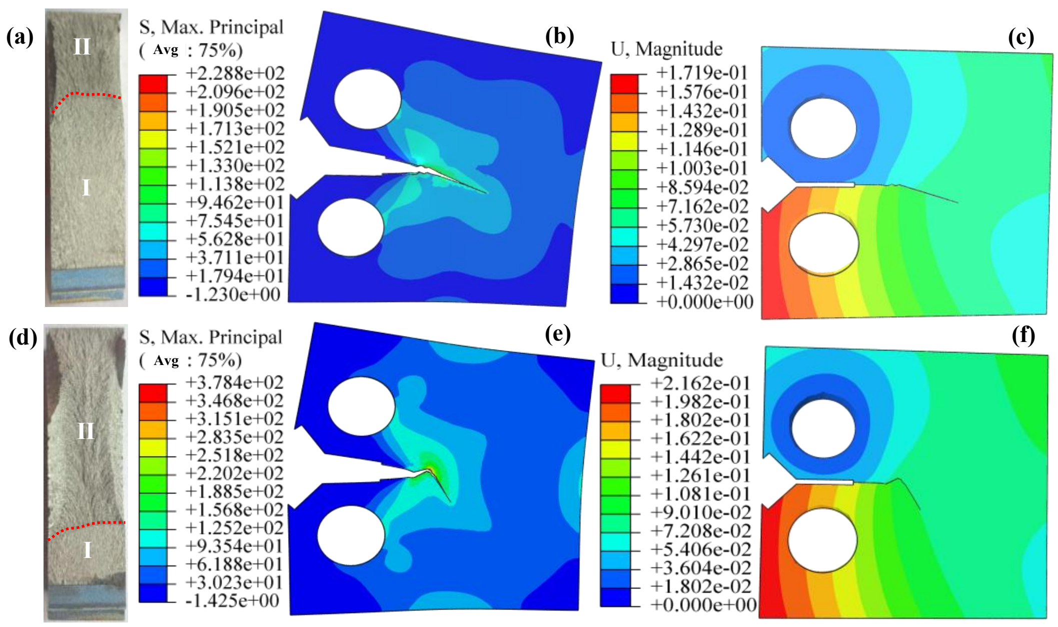

Fig. 14. (a-d) The macroscopic crack propagation path and fracture behavior of specimens A (a-c) and D (d-f) after da/dN test; (b) and (e) stress distribution near the crack tip; (f) and (e) the distribution of the U displacement cloud map.

However, the crisscrossing α_{fine} significantly impede the crack, leading to a non-periodic, oscillatory crack propagation process. This finding is consistent with the analysis of K_{IC}, which indicate that the crack propagation in specimen D consumes a greater amount of energy. Moreover, the presence of α_{fine} promotes the accumulation and retention of dislocations at the crack tip, enhancing local deform-ability. This effect leads to a wider region of deformation near the crack tip, causing blunting of the crack tip and hindering further crack propagation (Fig. 12). Therefore, the size and precipitation density of α_{fine} play a crucial role in influencing K_{IC} by indirectly impacting the level of plastic deformation at the crack tip.

5. Conclusions

(1) The inadequate driving force of phase transition retains a portion of the original equiaxial α phase (α_{eq}) at lower forging heating temperatures, which affects the content of α_{eq} in the trimodal microstructure. Prolonging the forging holding time or raising the forging heating temperature enhances the content of α_{lath} and fosters the growth of α_{fine}. Nevertheless, this does not lead to an increase in α_{eq} content.

(2) Increasing the forging heating temperature boosts strength by facilitating the strengthening effect at the interfaces through abundant α_{lath} content. Conversely, prolonging the forging duration adversely affects both plasticity and strength, primarily attributed to the reduction in α_{fine} content. The analysis based on Hall-Petch formula proves that α_{lath} parameters significantly affect forging strength. However, ductility is more affected by α_{eq} content.

(3) The combined deformation and fracture of α_{lath} and α_{fine} play a significant role in affecting initiation and propagation of impact cracks. Compared to α_{eq}, α_{lath} has lower dislocation free energy and fracture energy, promoting localized plastic deformation and shear fracture. The presence of α_{fine} further hinders dislocations, leading to increased impact energy.

(4) Cracks tends to take shorter propagation paths bypass α_{eq} with smaller aspect ratios. However, the α_{lath} with a high aspect ratio and a small thickness leads to a shorter slip distance, which increases the induced local plastic strain and promotes

crack propagation through α_{lath}, ultimately affecting K_{IC} values. Furthermore, the α_{fine} also affects the size of the plastic deformation zone at the crack tip and plays a key role in determining the deflection frequency and the local plastic deformation zone.

Declaration of competing interest

The authors affirm no competing financial interests or personal relationships that could have influenced the reported work.

Acknowledgments

This work was supported by the National Natural Science Foundation of China (Nos. 52061005 and 52261025), the Science and Technology Program of Guizhou Province (Nos. YQK[2023]009, [2021]310, and [2023]278). We also thank Dr. Xuehao Zheng from ZKKF (Beijing) Science & Technology Company for supporting of TEM analysis.

References:

[1] D. Banerjee, J. C. Williams, Perspectives on Titanium Science and Technology, Acta. Mater., 61 (2013), 844-879.

[2] D. Zhang, D. Qiu, Mark A Gibson, Y. Zheng, Hamish L Fraser, David H StJohn, Mark A Easton. Additive manufacturing of ultrafine-grained high-strength titanium alloys. Nature, 576 (2019), 91-95.

[3] C. Li, L. Huang, C. Li, S. Hui, Y. Yu, M. Zhao, S. Guo, J. Li. Research progress on hot deformation behavior of high-strength beta titanium alloy: flow behavior and constitutive model, Rare. Metals, 41 (2022), 1434-1455.

[4] Y. Wang, S. Xiu, S. Zhang, C. Jiang, Effect of grinding parameters on microstructure evolution of TC21 titanium alloy with bimodal starting microstructure, J. Alloy. Compd., 831 (2020), 154882.

[5] Q. Zhao, Q. Sun, S. Xin, Y. Chen, C. Wu, H. Wang, J. Xu, M. Wan, W. Zeng, Y. Zhao, High-strength titanium alloys for aerospace engineering applications: A review on melting-forging process, Mater. Sci. Eng. A., 845 (2022), 143260.

[6] X. Zhang, W. Jia, X. Mao, Effect of microstructure on the tensile properties and impact toughness of TC21G titanium alloy, Mater. Charact., 185 (2022), 111752.

[7] W. Zhu, C. Tan, R. Xiao, Q. Sun, J. Sun, Slip behavior of Bi-modal structure in a metastable β titanium alloy during tensile deformation, Mater. Sci. Eng. A, 57 (2020) 188-196.

[8] X. Xu, L. Dong, H. Ba, Z. Zhang, R. Yang, Hot deformation behavior and microstructural evolution of beta C titanium alloy in β phase field, T. Nonferr. Metal. Soc., 26 (2016), 2874-2882.

[9] Y. Zhang, S. Zhang, Z. Zou, Y. Shi, Achieving an ideal combination of strength and plasticity in additive manufactured Ti–6.5Al–2Zr–1Mo–1V alloy through the development of tri-modal microstructure, Mater. Sci. Eng. A., 840 (2022), 142944.
[10] Z. Shi, R. Liu, X. Wang, Z. Yao, Microstructure and mechanical properties of TC21 titanium alloy by near-isothermal forging, T. Nonferr. Metal. Soc., 25 (2015), 72-79.
[11] X. Zhou, W. Liu, F. Hao, Y. Mao, Y. Lai, Z. Zhao, Influence of quasi-β forging process on microstructure and properties of TC21 titanium alloy large forgings, Forging & Stamping Technology, 45 (2020), 29-34+44.
[12] L. Meng, T. Kitashima, T. Tsuchiyama, M. Watanabe, Effect of α precipitation on β texture evolution during β-processed forging in a near-β titanium alloy, Mater. Sci. Eng. A., 771 (2020), 138640.
[13] C. Huang, Y. Zhao, S. Xin, W. Zhou, Q. Li, W. Zeng, Effect of microstructure on tensile properties of Ti–5Al–5Mo–5V–3Cr–1Zr alloy, J. Alloy. Compd., 693 (2017), 582-591.
[14] X. Wen, M. Wan, C. Huang, M. Lei, Strength and fracture toughness of TC21 alloy with multi-level lamellar microstructure, Mater. Sci. Eng. A., 740-741 (2019), 121-129.
[15] S. Wang, Y. Liang, H. Sun, X. Feng, C. Huang, Thermomechanical treatment-induced microstructure refinement to optimize mechanical properties of TC21 titanium alloys, Mater. Sci. Eng. A, 812 (2021), 141095.
[16] C. Tan, Q. Sun, G. Zhang, Role of microstructure in plastic deformation and crack propagation behaviour of an α/β titanium alloy, Vaccum, 183 (2021), 109848.
[17] X. Wen, M. Wan, C. Huang, Y. Tan, M. Lei, Y. Liang, X. Cai, Effect of microstructure on tensile properties, impact toughness and fracture toughness of TC21 alloy, Mater. Des., 180 (2019), 107898.
[18] X. Ye, M. Wan, C. Huang, M. Lei, S. Jian, Y. Zhang, D. Xu, F. Huang, Effect of aging temperature on mechanical properties of TC21 alloy with multi-level lamellar microstructure, Mater. Sci. Eng. A, 840(2022), 142825.
[19] J. Wang, X. Ye, Y. Li, M. Wan, C. Huang, F. Huang, M. Lei, D. Liu, R. Ma, X. Ren, Effect of annealing temperature on mechanical properties of TC21 titanium alloy with multilevel lamellar microstructure, Mater. Sci. Eng. A, 869 (2023), 144788
[20] H. Shao, D. Shan, Y. Zhao, P. Ge, W. Zeng, Accordance between fracture toughness and strength difference in TC21 titanium alloy with equiaxed microstructure, Mater. Sci. Eng. A, 664 (2016), 10-16.
[21] Q. Meng, J. Xu, H. Li, C. Zhao, J. Qi, F. Wei, Y. Sui, W. Ma, Phase transformations and mechanical properties of a Ti36Nb5Zr alloy subjected to thermomechanical treatments, Rare. Metals, 41 (2022) 209-217.
[22] O. Ivasishin, P. Markovsky, Y. Matviychuk, S. Semiatin, C.H. Ward, S. Fox, A comparative study of the mechanical properties of high-strength β-titanium alloys, J. Alloy. Compd., 457 (2008) 296-309.

[23] Z. Tarzimoghadam, S. Sandlöbes, K. Pradeep, D. Raabe, Microstructure design and mechanical properties in a near-α Ti-4Mo alloy, Acta. Mater., 97 (2015) 291-304.
[24] Q. Yang, M. Ma,Y. Tan, S. Xiang, F. Zhao, Y. Liang, Microstructure and texture evolution of TB8 titanium alloys during hot compression, Rare. Metals, 40 (2021), 2917-2926.
[25] L. Chen, Q. Sun, L. Xiao, X. Zhao, Y. Xu, S. Zhang, P. Lyu, S. Fang, Effect of the subsolvus and supersolvus solution treatments on the basket-weave microstructure, room and high temperature properties of TC21 alloy, Mater. Sci. Eng. A, 893 (2024), 146150.
[26] Y. Zhang, R. Xin, B. Guo, K. Wang, Q. Liu, Influence of alternate grain boundary α on the development of Widmanstätten microstructure in TC21 Ti alloy, Mater. Charact., 177 (2021), 111162.
[27] C. Huang, F. Wang, X. Wen, M. Wan, M. Lei, J. Ye, W. Zeng, Tensile performance and impact toughness of Ti-55531 alloy with multilevel lamellar microstructure, J. Mater. Sci., 56 (2021), 8848-8870.
[28] L. Lei, Q. Zhao, Y. Zhao, S. Huang, C. Wu, W. Jia, W. Zeng, Study on the intrinsic factors determining impact toughness of TC21 alloy, Mater. Charact., 177 (2021), 111164.
[29] M. Hiroshi, T. Hirobumi, S. Eiichi, S. Yoshito,U. Shigeharu, Transgranular dislocation activities and substructural evolutions accommodating two-dimensional grain boundary sliding in ODS ferritic steel, Acta. Mater., 132 (2017), 245-254.
[30] M. Niinomi, T. Kobayashi, N. Sasaki, Toughness and microstructural factors of Ti-6Al-4V alloy, Mater. Sci. Eng. A, 100 (1988), 45-55.
[31] C. Wu, M. Zhan, Microstructural evolution, mechanical properties and fracture toughness of near β titanium alloy during different solution plus aging heat treatments, J. Alloy. Compd., 805 (2019), 1144-1160.
[32] C. Tan, X. Li, Q. Sun, L. Xiao, Y. Zhao, J. Sun, Effect of α-phase morphology on low-cycle fatigue behavior of TC21 alloy, Int. J. Fatigue, 75 (2015), 1-9.
[33] Y. Alshammari, M. Jia, F. Yang, L. Bolzoni, The effect of α+ β forging on the mechanical properties and microstructure of binary titanium alloys produced via a cost-effective powder metallurgy route, Mater. Sci. Eng. A, 769 (2020), 138496.
[34] W. Long, M. Ou, X. Mao, Y. Liang. In situ deformation behavior of TC21 titanium alloy with different alpha morphologies (equiaxed/lamellar). Rare. Metals, 40 (2021), 1173-1181.
[35] H. Li, K. Wang, L. Xin, R. Xin, Q. Liu, Effect of hot rolling and annealing on phase component, recrystallization, and mechanical properties of TC21 titanium alloy, J. Mater. Eng. Perform., 31 (2022), 2496-2508.
[36] Z. Lei, P. Gao, H. Li, Y. Cai, M. Zhan, On the fracture behavior and toughness of TA15 titanium alloy with tri-modal microstructure, Mater. Sci. Eng. A, 753 (2019), 238-246.

[37] H. Arabi, M. Ketabchi, S. Alhosseini, Mechanical and microstructural variations in ECAP of Ti-6Al-4V alloy with equiaxed microstructure, Rare Metals, 41(2022) 2732–2738.
[38] H. Matsumoto, H. Yoned, K. Sato, S. Kurosu, E. Mairec, D. Fabregue, T.J. Konno, A. Chiba, Room-temperature ductility of Ti-6Al-4V alloy with martensite microstructure, Mater. Sci. Eng. A, 528 (2011), 1512-1520.
[39] Y. Jiang , Y.C. Lin, X. Jiang , D. He , X. Zhang , N. Kotkunde, Hot tensile properties, microstructure evolution and fracture mechanisms of Ti-6Al-4V alloy with initial coarse equiaxed phases, Mater. Charact., 163 (2020), 110272.
[40] G. Chi, D. Yi, B. Jiang, L. Yang, H. Liu. Crack propagation during Charpy impact toughness testing of Ti−Al−V−Mo−Zr alloy tubes containing equiaxed and lamellar microstructures. J. Alloy. Compd., 852 (2021), 156581.
[41] D. Zhou, W. Zeng, J. Xu, S. Wang, W. Chen, Evolution of equiaxed and lamellar α during hot compression in a near alpha titanium alloy with bimodal microstructure, Mater. Charact., 151 (2019), 103-111.
[42] Y. Cui, W. Zheng, C. Li, G. Cao, Y. Wang, Effectiveness of hot deformation and subsequent annealing for beta grain refinement of Ti-5Al-5Mo-5V-1Cr-lFe titanium alloy, Rare Metals, 40 (2021), 3608–3615.
[43] J. Réthoré, A. Gravouil, A. Combescure, An energy-conserving scheme for dynamic crack growth using the extended finite element method, Int. J. Numer. Meth. Eng., 63 (2005), 631-659.
[44] C. Chen, D. Shang, N. Xiao, X. Li, A. Sha, J. Li, J. Li, Z. Tang, Z. Han, Y. Guo, D. Li, Fatigue life prediction of Ti60 titanium alloy under very high cycle loading at different temperatures, Int. J. Fatigue, 176 (2023), 107838.
[45] I. Marines-Garcia, P.C. Paris, H. Tada, C. Bathias, Fatigue crack growth from small to long cracks in very-high-cycle fatigue with surface and internal “fish-eye” failures for ferrite-perlitic low carbon steel SAE 8620, Mater. Sci. Eng. A, 468–470 (2007), 120-128.
[46] H. Gao, J. Zhan, B. Yu, W. Li, Z. Lin, H. Shang, Multi-scale characterization of fatigue crack tip deformation and propagation in QP steel, Mater. Charact., 210 (2024), 113822.